

# The encapsulation of particles and bubbles by an advancing solidification front

By MIN S. PARK, ALEXANDER A. GOLOVIN  
AND STEPHEN H. DAVIS

Department of Engineering Science and Applied Mathematics, Northwestern University,  
Evanston, IL 60208, USA

(Received 16 May 2005 and in revised form 19 January 2006)

An insoluble particle, a solid sphere or a spherical bubble, submerged in a liquid and approached by an advancing solidification front, may be captured by the front or rejected. The particle behaviour is determined by an interplay among van der Waals interactions, thermal conductivity differences between the particle and the melt, solid–liquid interfacial energy, the density change caused by the liquid–solid phase transition, and in the case of a bubble, the Marangoni effect at the liquid–gas interface. We calculate the particle velocity and the deformation of the front when the particle is close to the front, using the lubrication approximation, and investigate how the particle speed, relative to the front, depends on the parameters that characterize the described effects.

---

## 1. Introduction

The interaction between particles and solidification fronts is important for many applications. It affects the quality of large crystals grown by directional solidification; it is crucial for fabrication of composites reinforced by particles and determines their effective bulk properties (Shangguan, Ahuje & Stefanescu 1992); it governs the formation of ice lenses in frozen soils (Corte 1962); and last but not least, it is the key process in the cryo-preservation of biological cells (Bronstein, Itkin & Ishkov 1981; Körber 1988).

When a solidification front approaches a particle (solid particle, bubble, biological cell, etc.) that is suspended in a melt near the front, it can either repel the particle, pushing it in front of itself, or it can engulf the particle, trapping it within the growing solid region. The outcome of this interaction depends on the speed of the solidification front, the particle size and various physical characteristics of the particle–melt–crystal system.

Corte (1962), motivated by geological applications, carried out the first experiments on the interaction of an ice–water interface with different solid particles and reported the first experimentally observed relation between the solidification speed and the particle size. Uhlmann, Chalmers & Jackson (1964) suggested that the particle–front interaction is determined by the particle material properties and its size, owing to the change of chemical potential of the liquid between the particle and the solidification front. They assumed that the particle engulfment occurs when the separation distance becomes of the order of one molecular diameter.

Chernov, Temkin & Mel'nikova (1976) explained that the interaction between a particle and a solidification front is governed by the van der Waals interactions that

repel the particle from the interface; the particle speed is then determined by the balance between the van der Waals and the viscous lubrication forces caused by the flow of liquid around the particle. Under the assumption of a paraboloid frontal shape near the particle Chernov *et al.* (1976) derived an approximate analytical expression for the particle speed as a function of its size, the temperature gradient and the solid–liquid surface energy that affects the phase equilibrium conditions due to the Gibbs–Thomson relation. Similar treatment of the problem was proposed by Gilpin (1980) who, however, adopted the earlier approach by Uhlmann *et al.* (1964) based on the change of the chemical potential. It is now generally accepted that the interplay between the van der Waals and lubrication forces plays the key role in the particle–front interaction. An asymptotic analysis of the frontal shape for the case when a particle is very close to the front was performed by Hadji (1999, 2002) who considered the effects of van der Waals and lubrication forces combined with the Gibbs–Thomson effect. These analyses were generalized by Rempel & Worster (1999, 2001) who also took into account the shift of the phase equilibrium caused by the disjoining pressure.

Another important factor that affects the particle behaviour near an advancing solidification front is the difference of thermal conductivities of the particle, melt and solid. Zubko, Lobanov & Nikonova (1973) experimentally examined the influence of the thermal parameters on the capture of a particle using naphthalene and particles of low-melting-point metals with different thermal conductivities. It was found that the ratio of thermal conductivities of the particle and the melt was one of the main factors that determined the behaviour of a particle near a growing crystal. Chernov, Temkin & Mel'nikova (1977) were the first to explain this observation as due to the distortion of the isotherms around a particle whose thermal conductivity differs from that of the surrounding melt and the adjacent crystal. They showed that if the particle heat conductivity is less than that of the solid and melt (assumed equal) this leads to the formation of a bulge at the solid–liquid interface that repulses the particle. In the opposite case, when the particle heat conductivity is larger than that of the melt and solid, this leads to the formation of a depression at the front that promotes the particle capture.

Sen *et al.* (1997), using X-ray transmission microscope, observed real-time evolution of the shape of a solidification front moving towards particles with different thermal conductivities. They found that thermal effects associated with thermal conductivity differences affect the maximum speed of the particle near the front, resulting in the engulfment of high-conductivity particles and rejection of low-conductivity ones. The effects of thermal conductivities of a particle, melt and solid on the interaction between a particle and a solidification front were reviewed by Azouni & Casses (1998). A summary of various theoretical models and experimental correlations describing the conditions for particle engulfment is given in Stefanescu *et al.* (1999) and Catalina, Mukherjee & Stefanescu (2000). Numerical simulations of a free-boundary problem describing the behaviour of a spherical solid particle near an advancing solidification front were performed recently by Garvin & Udaykumar (2003*a, b*, 2004, 2005).

While the behaviour of solid particles near advancing solidification fronts has received much attention, the interaction between solidification fronts and gas bubbles has been much less studied. The main effect that distinguishes the behaviour of a bubble near a solidification front from a solid particle is the thermocapillary effect caused by the dependence of the bubble surface tension on temperature. In the presence of temperature gradient this effect results in the migration of a bubble in the direction of the gradient that is caused by the flow produced by the gradient of

the surface tension (Young, Goldstein & Block 1959). Bagdasarov, Okinshevich & Kholov (1980) first included the thermocapillary effect in the force equilibrium and, using the balance of a body force, lubrication force, and thermocapillary force, calculated the critical speed of the solidification front at which the bubble capture occurs. Geguzin & Dzyuba (1981) considered the temperature gradient on the bubble surface and calculated the bubble velocity by using the balance of intermolecular force and viscous resistance with thermocapillary effect. Dzyuba & Zu (1985) considered the velocity of bubble thermocapillary motion near a solidification front and obtained the dependence of the gap between the particle and the front on the bubble radius and the surface tension gradient. An effect similar to thermocapillary but caused by a concentration gradient can occur if a substance that changes the bubble surface tension (surfactant) is present in the melt. This concentration–capillary effect was investigated experimentally by Wang, Mukai & Lee (1999) who showed that the gradient of surfactant concentration near a solidification front can cause bubble motion towards the front and promote engulfment.

Another important effect that can have a large influence on the interaction between a particle and a solidification front is the bulk flow caused by the density variation upon solidification. Depending on whether the density of the solid is larger or smaller than that of the melt, the flow can be towards or away from the front, directly affecting the particle. The effect of the density-variation-driven flow on particle engulfment has not yet been studied.

In the present study we generalize the analysis of the interaction between a particle (solid particle or a gas bubble) and an advancing solidification front for the case when all the effects described above are present. We investigate the relative importance of various effects in the presence of others and draw a unified picture of engulfment. The main goal of this paper is to derive conditions for a particle (a droplet or a bubble) to be engulfed by an advancing solidification front or to be repelled by it. These conditions are determined by the particle velocity relative to the planar parts of the front far from the particle: the particle will be engulfed if, as a result of the front–particle interaction, the particle moves towards the front. Here, we study this problem by means of an asymptotic analysis in the lubrication approximation, valid in the case when the separation distance between the front and the particle is much less than the particle radius and when the variations of the frontal shape near the particle are small. In this approximation, we compute the particle velocity resulting from the balance of hydrodynamic, intermolecular and other forces acting between the particle and the front. Comparing this velocity with that of planar parts of the advancing solidification front far from the particle allows us to find the conditions for particle engulfment.

## 2. Formulation of the model

In the present work the term particle will denote either a solid sphere or a spherical bubble. Consider a particle of radius  $R$  suspended in a pure liquid while a solidifying front approaches it at speed  $V$ . The frame of reference in which the solidification front is moving with speed  $V$  will be referred to as the lab frame. We consider here the situation typical of *directional solidification* in which the frontal speed is prescribed by the pulling of the melt through an applied temperature gradient, positive in the direction from the solid to the liquid. The particle is initially positioned with its centre at a distance  $H$  from the melting-temperature isotherm at  $T = T_m$  (see figure 1). When  $H - R$  is about 100 nm, van der Waals interactions become effective. If the van

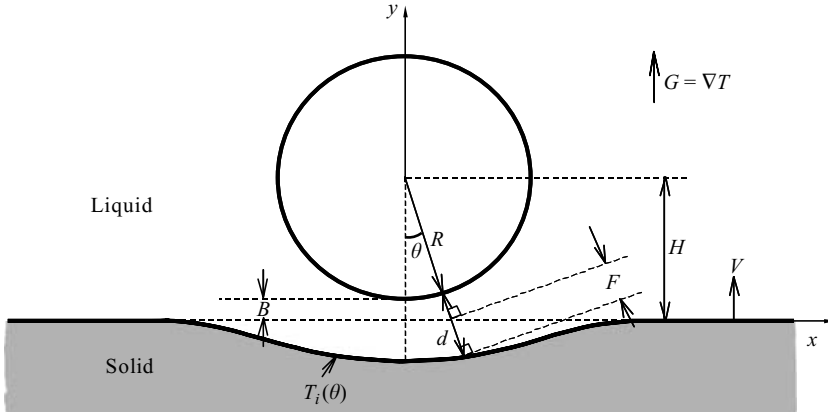


FIGURE 1. A spherical particle near a moving solidification front in a temperature gradient  $G$ . The particle is separated from the solid–liquid interface by a film of melt of thickness  $d(\theta)$ .

der Waals interactions are repulsive (and we consider only this case), they push the particle away from the front and the disjoining pressure in the gap between the particle and the front results in front deformation. Note that besides van der Waals interactions other repulsive interactions can be important, e.g. electrostatic or double-layer, see Israelachvili (1992). The particle speed is determined by the balance between the disjoining pressure and the lubrication pressure. The latter depends on the flow in the gap between the particle and the front as well as on the boundary conditions on the particle surface (no-slip in the case of a solid particle and no-stress or thermocapillary stress in the case of a bubble). The lubrication pressure is also affected by the bulk flow produced by the density change upon solidification, as well as by the shape of the front. The latter, in turn, depends on many factors, such as the temperature field, the thermal conductivities of three different phases, crystal–melt surface energy and the disjoining pressure in the gap between the particle and the front.

In the presence of the disjoining pressure caused by the van der Waals interactions, the solid–liquid equilibrium temperature  $T_i$  of a curved front is given by the Gibbs–Thomson equation,

$$T_i = T_m \left[ 1 - \left( \frac{\lambda}{d} \right)^3 - \frac{\sigma \mathcal{H}}{L_v} \right], \quad (2.1)$$

where  $\mathcal{H}$  is the front curvature,  $\sigma$  is the front interfacial energy,  $L_v$  is the latent heat per unit volume of solid,  $d$  is the film thickness between the particle and the front and  $\lambda$  is the disjoining pressure length scale (Wettlaufer *et al.* 1996) defined by

$$\lambda = \left( \frac{A}{6\pi L_v} \right)^{1/3}, \quad (2.2)$$

where  $A$  is the Hamaker constant characterizing the van der Waals interactions between the material of the particle and the solid separated by a planar liquid film (Israelachvili 1992).

Here we make the following assumptions: the Péclet number  $Pe = UR/\kappa_T \ll 1$  ( $U$  is the particle speed and  $\kappa_T$  is the melt thermal diffusivity) so that the convective heat transfer can be neglected (for typical values  $V \sim 10^{-6} \text{ m s}^{-1}$ ,  $R \sim 10^{-6} \text{ m}$ ,  $\kappa_T \sim 10^{-7} \text{ m}^2 \text{ s}^{-1}$ ,  $Pe \approx 10^{-5}$ ); the thermal conductivities of the melt and the crystal are

equal; latent heat is neglected in the heat balance; the applied temperature gradient  $G$  is constant; the particle remains spherical (for a bubble with typical values  $\sigma = 0.05 \text{ J m}^{-2}$ ,  $\rho = 10^3 \text{ kg m}^{-3}$ ,  $U \sim 10^{-6} \text{ m s}^{-1}$ , the Weber number  $We = \sigma/\rho U^2 R \sim 5 \times 10^{13} \gg 1$  and therefore the bubble deformation can be neglected†). Under these assumptions, the interface temperature can be written as (Chernov *et al.* 1977)

$$T_i(\theta, t) = T_0 - G(R + d) \cos \theta \left[ 1 + k_e \left( \frac{R}{R + d} \right)^3 \right] - G \int_0^t [V - U(\tau)] d\tau, \quad (2.3)$$

where  $T_0$  is the temperature at the centre of the particle (see figure 1),  $U(\tau)$  is the particle velocity in the lab frame, and

$$k_e = \frac{k_m - k_p}{2k_m + k_p}, \quad (2.4)$$

where  $k_m$  and  $k_p$  are heat conductivities of the melt and particle, respectively; thus  $-1 \leq k_e \leq 1/2$ .

It is convenient to choose the characteristic length scale (Rempel & Worster 1999)

$$l \equiv (\lambda^3 T_m / G)^{1/4} = \left( \frac{AT_m}{6\pi L_v G} \right)^{1/4}, \quad (2.5)$$

and combine equations (2.1) and (2.3) to obtain

$$\Gamma R \mathcal{K} + \frac{l^4}{d^3} = (R + d) \cos \theta \left[ 1 + k_e \left( \frac{R}{R + d} \right)^3 \right] - H, \quad (2.6)$$

where

$$\Gamma = \frac{T_m \sigma}{L_v G R} \quad (2.7)$$

is the capillary length, and

$$H = \frac{T_0 - T_m}{G} - \int_0^t [V - U(\tau)] d\tau. \quad (2.8)$$

Note that here  $d = d(\theta)$ ,  $d(0) = d_0$ ; see figure 1.

Since the film thickness above the deformed front is much less than  $R$ , the disjoining pressure can be taken as

$$P_T = \frac{A}{6\pi d^3} = \frac{L_v \lambda^3}{d^3}, \quad (2.9)$$

where  $A$  is the Hamaker constant. The total van der Waals force on the particle is calculated by integrating  $P_T$  over the particle surface. For a spherical particle near the front, the normal component of this force is given as

$$F_T = 2\pi R^2 \int_0^{\theta_c} P_T \sin \theta \cos \theta d\theta = \pi R^2 L_v \frac{Gl^4}{T_m} \int_0^{\theta_c} \frac{\sin(2\theta)}{d^3(\theta)} d\theta. \quad (2.10)$$

Because the film thickness increases rapidly with  $\theta$ , the largest contributions to  $F_T$  come from the region near the base of the particle. If the integration limit  $\theta_c$  is such that the film thickness at  $\theta_c$  is much greater than the film thickness  $d_0$  immediately

† The bubble can deform during its capture by the solid phase but this process is not described by our model.

beneath the particle, the value of the integral will only very weakly depend on  $\theta_c$ . Thus, for the numerical calculations that follow, we use  $\theta_c \rightarrow \pi/2$ .

When the particle moves, flow occurs in the thin film that separates the particle from the front. Near the base of the particle a lubrication approximation can be used to find the volume flux; the latter depends on whether the particle is a solid sphere or a bubble. The equation of the lubrication approximation is given by

$$\mu \frac{\partial^2 u}{\partial \bar{y}^2} = \frac{\partial P}{\partial \bar{x}}, \quad (2.11)$$

where  $u$  is the tangential component of the flow velocity in the film,  $P$  is pressure,  $\mu$  is the dynamic viscosity of the liquid, and the coordinates  $\bar{x}$  and  $\bar{y}$  differ from the coordinates  $x$  and  $y$  shown in figure 1 by the choice of the origin: here it is at the solid–liquid interface, at the point corresponding to the minimal gap between the particle and the front. Using the no-slip boundary condition at the solidification front, and at the surface of a solid particle, the flow velocity in the film is obtained as

$$\bar{u} = \frac{1}{2\mu} \frac{\partial P}{\partial \bar{x}} \bar{y}(\bar{y} - d). \quad (2.12)$$

Integrating  $\bar{u}$  from 0 to  $d$  gives the volume flux

$$q_p = -\frac{\pi d^3(\theta)}{6\mu} \sin \theta \frac{dP}{d\theta}. \quad (2.13)$$

Note that this is the volume flux of liquid out of the gap between the particle and the front, so it is negative if the particle is moving away from the front and the liquid is flowing into the gap.

In the case of a bubble, the thermal gradient generates thermocapillary stress at the bubble–melt interface that is balanced by the shear stress,

$$\mu \frac{\partial \bar{u}}{\partial \bar{y}} = \frac{\partial \sigma}{\partial \bar{x}} = \frac{\partial \sigma}{\partial T} \frac{\partial T}{\partial \bar{x}} = -\beta \frac{\partial T}{\partial \bar{x}}. \quad (2.14)$$

In this case one obtains for the velocity

$$\bar{u} = \frac{1}{2\mu} \frac{\partial P}{\partial \bar{x}} (\bar{y}^2 - 2d\bar{y}) - \frac{\beta}{\mu} \frac{\partial T}{\partial \bar{x}} \bar{y} \quad (2.15)$$

and for the volume flux

$$q_b = -\frac{2\pi d^3(\theta)}{3\mu} \sin \theta \frac{\partial P}{\partial \theta} + \frac{\pi\beta}{\mu} \sin \theta \frac{\partial T}{\partial \theta} d^2(\theta), \quad (2.16)$$

where  $\beta = -\partial\sigma/\partial T$  is typically positive.

Regardless of the density difference between the melt and the solid, mass conservation implies that the volume of liquid transported past the angular position  $\theta$  in a time  $dt$  is equal to the volume swept out beneath the particle as it travels the corresponding distance  $dz$ . Liquid of density  $\rho_l$  becomes solid of density  $\rho_s$  upon solidification, e.g. there is contraction in metals and expansion in water and semiconductors. Conservation of mass should additionally take into account the volume proportional to the rate of volume contraction (or expansion) due to solidification which is equal the volume swept in (or out) beneath the particle as the front travels the additional distance  $d\zeta$  proportional to the change of volume. The balance of mass in the liquid film is given by

$$q dt = -\pi(R \sin \theta)^2 dz + \pi[(R + d) \sin \theta]^2 d\zeta, \quad (2.17)$$

where  $d\zeta = V(1 - \rho_s/\rho_l) dt$ . Combining this with equations (2.13) and (2.16) allows the lubrication pressure to be written for the solid

$$P_p = 6\mu R^2 U \int_{\theta_c}^{\theta} \frac{\sin \phi}{d^3(\phi)} d\phi - 6\mu V \rho' \int_{\theta_c}^{\theta} \frac{[R + d(\phi)]^2 \sin \phi}{d^3(\phi)} d\phi, \quad (2.18)$$

and the bubble

$$P_b = \frac{3}{2}\mu R^2 U \int_{\theta_c}^{\theta} \frac{\sin \phi}{d^3(\phi)} d\phi - \frac{3}{2}\beta \int_{\theta_c}^{\theta} \frac{\partial T}{\partial \phi} \frac{d\phi}{2d(\phi)} - \frac{3}{2}\mu V \rho' \int_{\theta_c}^{\theta} \frac{[R + d(\phi)]^2 \sin \phi}{d^3(\phi)} d\phi, \quad (2.19)$$

where  $U \equiv dz/dt$  is the particle velocity,  $V$  is the speed of the solidification front, and  $\rho' = 1 - \rho_s/\rho_l$ .

The normal component of the lubrication force is found by integrating the liquid pressure over the particle surface; for the solid particle

$$F_{\mu,p} = 6\pi\mu R^4 U \int_0^{\theta_c} \sin 2\theta d\theta \int_{\theta_c}^{\theta} \frac{\sin \phi}{d^3(\phi)} d\phi - 6\pi\mu R^2 V \rho' \int_0^{\theta_c} \sin 2\theta d\theta \int_{\theta_c}^{\theta} \frac{[R + d(\phi)]^2 \sin \phi}{d^3(\phi)} d\phi, \quad (2.20)$$

and for the bubble

$$F_{\mu,b} = \frac{3}{2}\pi\mu R^4 U \int_0^{\theta_c} \sin 2\theta d\theta \int_{\theta_c}^{\theta} \frac{\sin \phi}{d^3(\phi)} d\phi - \frac{3}{2}\pi R^2 \beta \int_0^{\theta_c} \sin 2\theta d\theta \int_{\theta_c}^{\theta} \frac{\partial T}{\partial \phi} \frac{d\phi}{d(\phi)} - \frac{3}{2}\pi\mu R^2 V \rho' \int_0^{\theta_c} \sin 2\theta d\theta \int_{\theta_c}^{\theta} \frac{[R + d(\phi)]^2 \sin \phi}{d^3(\phi)} d\phi. \quad (2.21)$$

The front deformation is determined by the surface energy, disjoining pressure and different thermal conductivities of the phases. The effect of different thermal conductivities turns out to deform the front as much as  $10^3$  times more than the effect of the surface energy. It is therefore convenient to scale the distances  $F$  and  $B$  shown in figure 1 as  $f \equiv F/(\epsilon_s R)$  and  $b = B/(\epsilon_s R)$ , where  $\epsilon_s \equiv (l^4/\Gamma R^3)^{1/3} = (A/6\pi\sigma R^2)^{1/3}$ . The typical values of  $A \sim 10^{-20}$  J,  $\sigma \sim 10^{-2}$  J m<sup>-2</sup> and  $R \sim 10^{-6}$  m give  $\epsilon_s \sim 10^{-2}$ . Thus, we assume  $\epsilon_s \ll 1$  for micron-size and larger particles. Since the frontal deformation is significant in the region corresponding to a small angular distance from the particle base we shall define the perturbation of the film thickness as

$$f = \frac{1}{\epsilon_s R} \left( d - \frac{H - R \cos \theta}{\cos \theta} \right). \quad (2.22)$$

The film thickness is of the order of  $\epsilon_s R$  near the base of the particle and diverges towards infinity as  $\theta$  tends to  $\pi/2$ .  $F \equiv \epsilon_s R f$  is the radial distance from the position of the deformed solidification front to the solidification plane far away from the particle as shown in figure 1 and  $f$  changes from zero at the particle base to  $O(1)$  value far from it where the frontal shape is practically planar.

When the distance  $d$  between the particle and the front becomes small enough, the van der Waals interactions become important. We take  $H \equiv R + \epsilon_s R b$  where  $\epsilon_s \ll 1$  and  $b = O(1)$ , define a new variable,  $s \equiv 1 - \cos \theta$ ,  $0 < s < 1$ , and rewrite (2.6) in terms of  $f$  and  $s$ . One can divide the region between the particle and the front into two parts: the inner region, where the right-hand side of equation (2.6) is balanced mainly by the second term on the left-hand side describing the van der Waals interactions,

and the outer region, in which the right-hand side of equation (2.6) is balanced mainly by the first term on the left-hand side describing the Gibbs–Thomson relation. In the inner region  $s = O(\epsilon_s)$  while in the outer region  $s = O(1)$ .

The boundary conditions consist of the symmetry condition at  $\theta = 0$  and the requirement that the solidification front becomes planar far away from the particle so that

$$\frac{dd(\theta)}{d\theta} = 0 \text{ at } \theta = 0 \quad \text{and} \quad d \rightarrow \frac{H - R \cos \theta}{\cos \theta} \text{ as } \theta \rightarrow \frac{\pi}{2}. \quad (2.23)$$

In the outer region where the van der Waals interactions are negligible equation (2.6) can be reduced to

$$[(1-s)^4 - (1-s)^6]f'' - [3(1-s)^3 - 5(1-s)^5]f' + [(1-s)^2 - 3(1-s)^4]f = \frac{f}{\gamma}, \quad \gamma \equiv \Gamma/R, \quad (2.24)$$

where the prime denotes a derivative with respect to  $s$ . Equation (2.24) implies that the frontal shape in the outer region is determined by the effect of the surface energy. Also, it follows from (2.23) that  $f \rightarrow 0$  for  $s \rightarrow 1$ .

In the inner region  $s = O(1)$  and the leading-order approximation for the front deformation is given by

$$2(\xi f')' + \frac{1}{(\xi + b + f)^3} - \frac{k_e}{\gamma} = 0. \quad (2.25)$$

Here the prime denotes a derivative with respect to  $\xi \equiv s/\epsilon_s$ . Equation (2.25) implies that the frontal deformation in the inner region is determined by the combined effect of van der Waals interactions, the surface energy and different heat conductivities. The boundary condition at  $s = 0$  from equation (2.23) can be derived as

$$2f' + \frac{1}{(b + f)^3} - \frac{k_e}{\gamma} = 0 \quad \text{at} \quad \xi = 0. \quad (2.26)$$

In order to determine the shape of the interface we solve equations (2.24) and (2.25) numerically. First, we choose an initial estimate  $f_0$  to satisfy the boundary condition (2.26) that corresponds to  $dd/d\theta = 0$ . Equation (2.25) is then integrated by a Runge–Kutta method, from  $\xi = 0$  to  $\xi = \xi_2$ , where  $\xi_2$  is chosen between 1 and  $1/\epsilon_s$ . After that we use the values  $f(s_1) = f(\xi_2)$  and  $f'(s_1) = f'(\xi_2)/\epsilon_s$  at that point as initial conditions to integrate from  $s_1 = \epsilon_s \xi_2$  to  $s_2 < 1$ . The integration is terminated if  $f$  starts to blow up. We then improve the initial guess  $f_0$  by means of a bisection method. This allows us to choose the best approximation to the value of  $f_0$  (up to  $10^{-7}$ ) for which the far-field boundary condition,  $f \rightarrow 0$  as  $s \rightarrow 1$ , is satisfied.

### 3. Bubble velocity

We ignore buoyancy and set the sum of the lubrication, van der Waals and thermo-capillary forces to zero. This gives the velocity of the bubble in the form

$$U_b = 4U_1 + U_2 + U_3, \quad (3.1)$$

where

$$U_1 = -\frac{L_v \lambda^3}{6\mu R^2} I_0^{-1} \int_0^{\theta_c} d^{-3}(\theta) \sin 2\theta \, d\theta, \quad (3.2a)$$



Parameters	SiC in water	Air bubble in water	SiC in aluminum	Air bubble in aluminum
$A_{sw}$ (J)	$1.3 \times 10^{-19}$	$5.0 \times 10^{-21}$	$5.5 \times 10^{-19}$	$1.0 \times 10^{-20}$
$G$ ( $\text{K m}^{-1}$ )	$1.0 \times 10^4$	$1.0 \times 10^4$	$1.0 \times 10^4$	$1.0 \times 10^4$
$R$ (m)	$1.0 \times 10^{-6}$	$1.0 \times 10^{-6}$	$1.0 \times 10^{-6}$	$1.0 \times 10^{-6}$
$\rho_l$ ( $\text{kg m}^{-3}$ )	$9.98 \times 10^2$	$9.98 \times 10^2$	$2.38 \times 10^3$	$2.38 \times 10^3$
$\rho_s$ ( $\text{kg m}^{-3}$ )	$9.17 \times 10^2$	$9.17 \times 10^2$	$2.7 \times 10^3$	$2.7 \times 10^3$
$T_m$ (K)	273.15	273.15	933	933
$L_v$ ( $\text{J m}^{-3}$ )	$3.03 \times 10^8$	$3.03 \times 10^8$	$1.08 \times 10^9$	$1.08 \times 10^9$
$\sigma_{sl}$ ( $\text{J m}^{-2}$ )	$3.0 \times 10^{-2}$	$3.0 \times 10^{-2}$	$1.43 \times 10^{-1}$	$1.43 \times 10^{-1}$
$\mu$ (Pa s)	$1.8 \times 10^{-3}$	$1.8 \times 10^{-3}$	$4.0 \times 10^{-3}$	$4.0 \times 10^{-3}$
$k_m$ ( $\text{W m}^{-1} \text{K}$ )	$5.69 \times 10^{-1}$	$5.69 \times 10^{-1}$	$1.03 \times 10^2$	$1.03 \times 10^2$
$k_p$ ( $\text{W m}^{-1} \text{K}$ )	$4.2 \times 10^1$	$2.43 \times 10^{-2}$	$2.94 \times 10^1$	$6.27 \times 10^{-2}$
$V_{sl}$ ( $\text{m s}^{-1}$ )	$5.00 \times 10^{-7}$	$5.00 \times 10^{-7}$	$3.00 \times 10^{-7}$	$3.00 \times 10^{-7}$
$\beta$ ( $\text{Pa K}^{-1}$ )	—	$1.0 \times 10^{-5}$	—	$1.0 \times 10^{-5}$
$\lambda$ (m)	$2.83 \times 10^{-10}$	$9.57 \times 10^{-11}$	$3.00 \times 10^{-10}$	$7.89 \times 10^{-11}$
$\gamma$	2.71	2.71	12.4	12.4
$k_e$	-0.96	0.47	0.31	0.50
$M$	—	$8.75 \times 10^{-2}$	—	$6.05 \times 10^{-2}$
$N$	$4.46 \times 10^{-4}$	$5.14 \times 10^{-3}$	$-3.3 \times 10^{-4}$	$-6.67 \times 10^{-3}$

TABLE 1. Typical parameter values for use in predicting the behaviour of an insoluble particle near an advancing solidification front. The tabulated values for the effective Hamaker constant  $A_{sw}$  are from Johansen & Taniguchi (1998) and Onoda (1985).  $G$ ,  $R$ , and  $\lambda$  are referred to Rempel & Worster (2001),  $\beta$  are referred to Young *et al.* (1959), and the other thermodynamic properties are referred to Shackelford & Alexander (2000). Dependence of the thermal properties of air and SiC on temperature is taken into account.

$$U_2 = \frac{\beta}{\mu R^2} I_0^{-1} \int_0^{\theta_c} \sin 2\theta \, d\theta \int_{\theta_c}^{\theta} \frac{\partial T}{\partial \phi} d^{-1}(\phi) \, d\phi, \quad (3.2b)$$

$$U_3 = \rho' V I_0^{-1} \int_0^{\theta_c} \sin 2\theta \, d\theta \int_{\theta_c}^{\theta} [1 + d(\theta)/R]^2 \sin \phi \, d^{-3}(\phi) \, d\phi, \quad (3.2c)$$

$$I_0 = \int_0^{\theta_c} \sin 2\theta \, d\theta \int_{\theta_c}^{\theta} \sin \phi \, d^{-3}(\phi) \, d\phi, \quad (3.2d)$$

where the film thickness,  $d(\theta)$ , is determined from equation (2.6). It is convenient to introduce the following dimensionless variables:  $h = H/R$ ,  $\delta = d/l$ ,  $\gamma = \Gamma/R$  and  $\kappa = R\mathcal{H}$ . Using these, equation (2.6) can be written as

$$\gamma\kappa + \epsilon\delta^{-3} = [1 + \delta\epsilon + k_e(1 + \delta\epsilon)^{-2}] \cos \theta - h, \quad (3.3)$$

where  $\epsilon = l/R$ ; for a micron-size particle (see table 1),  $\epsilon \approx 10^{-2} \ll 1$ . To choose a velocity scale we recall the definition for  $l$  and let

$$W = \frac{L_v l^3 G}{6\mu T_m R} = \frac{1}{6\mu R} \left( \frac{L_v G}{T_m} \right)^{1/4} \left( \frac{A}{6\pi} \right)^{3/4}, \quad (3.4)$$

which is identical to that proposed by Chernov *et al.* (1976, 1977). Although, as shown by Rempel & Worster (2001), another scaling is more appropriate when the effects of the crystal–melt surface energy are important, we have chosen scale (3.4) in order to make the analysis of relative roles of various effects more transparent. From equation (3.1) the dimensionless bubble velocity becomes

$$u_b = 4u_1(\delta_0, \gamma, k_e) + Mu_2(\delta_0, \gamma, k_e) + Nu_3(\delta_0, \gamma, k_e), \quad (3.5)$$

where

$$u_1 = -\epsilon j_0^{-1} \int_0^{\theta_c} \frac{\sin 2\theta}{\delta^3(\theta)} d\theta, \quad (3.6a)$$

$$u_2 = j_0^{-1} \int_0^{\theta_c} \sin 2\theta d\theta \int_{\theta_c}^{\theta} \delta^{-1}(\phi) \sin \phi d\phi, \quad (3.6b)$$

$$u_3 = j_0^{-1} \int_0^{\theta_c} \sin 2\theta d\theta \int_{\theta_c}^{\theta} \frac{[1 + \epsilon\delta(\phi)]^2}{\delta^3(\phi)} \sin \phi d\phi, \quad (3.6c)$$

$$j_0 = \int_0^{\theta_c} \sin 2\theta d\theta \int_{\theta_c}^{\theta} \delta^{-3}(\phi) \sin \phi d\phi. \quad (3.6d)$$

$$M = \frac{6\beta T_m R}{L_v l^2}, \quad N = \frac{6\mu T_m R (\rho_l - \rho_s)}{L_v l^3 G \rho_l} V. \quad (3.6e)$$

The integrals (3.6a)–(3.6d) are evaluated using the function  $\delta(\theta)$  found from the numerical solution of (3.3). They are functions of the dimensionless gap  $\delta_0$  between the front and the bubble corresponding to the minimum of the melt film thickness, the surface-energy parameter,  $\gamma$ , and the thermal conductivity ratio parameter,  $k_e$ . The value of  $\delta_0$  is determined mainly by the balance between interfacial-curvature effects and van der Waals interactions. The dimensionless parameter  $M$  is the Marangoni number characterizing the thermocapillary effect, and the dimensionless parameter  $N$  characterizes the additional flow caused by the density change upon crystallization. Usually, for a micron-size particle,  $10^{-4} < N < 10^{-2}$ , so  $N \ll 1$  (see table 1) and since  $\epsilon \ll 1$ , one can just set  $u_3 \equiv 1$ . Note that for  $\gamma = 0$  (negligible effects of the surface energy), the functions  $u_1(\delta_0, 0, k_e)$  and  $u_2(\delta_0, 0, k_e)$  can be computed analytically. The corresponding formulae are given in the Appendix. Note also that for  $\gamma \rightarrow 0$  equations (2.24)–(2.26) become singularly perturbed and their solution develops a boundary layer. However, the rescaled frontal shape  $F$  tends to a specific limiting shape in this case (see also Rempel & Worster 2001).

#### 4. Solid-particle velocity

The analysis described above for a spherical bubble is easily applied to the case of a solid spherical particle. We neglect the buoyancy and set the sum of the intermolecular force and the lubrication force to zero, thus obtaining the following velocity for the solid particle:

$$U_p = U_1 + U_3, \quad (4.1)$$

where  $U_1$  and  $U_3$  are given by equations (3.2a) and (3.2c), respectively, and the film thickness can be determined from equation (2.6). Introducing dimensionless parameters as described in § 3.1, one obtains the dimensionless particle velocity,

$$u_p = u_1(\delta_0, \gamma, k_e) + N u_3(\delta_0, \gamma, k_e), \quad (4.2)$$

where  $u_1$  and  $u_3$  are given by equations (3.6a) and (3.6c), respectively; as for the case of a bubble, one can set  $u_3 \equiv 1$ .

#### 5. Results and discussion

The velocity  $u_p$  of a solid particle interacting with an advancing solidification front depends on  $\delta_0$ , which is determined by the balance between the van der Waals and lubrication forces, by  $\gamma$  that characterizes the effect of the surface energy of the

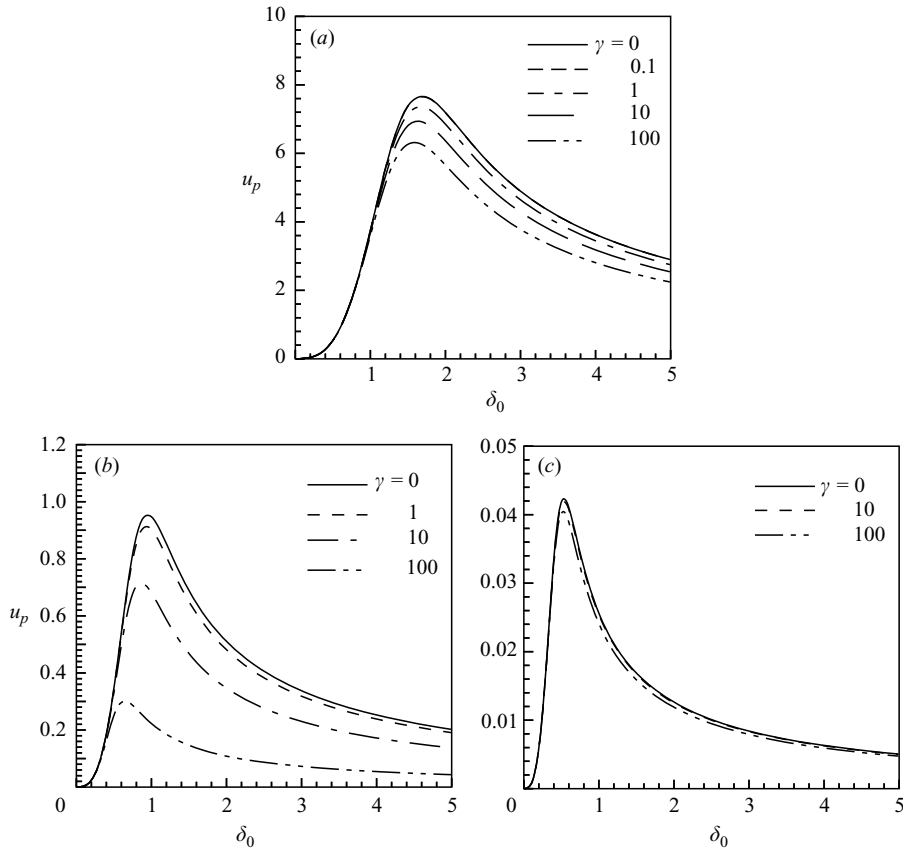


FIGURE 2. Dimensionless particle velocity  $u_p$  as a function of the dimensionless film thickness  $\delta_0$  for various values of the surface energy parameter  $\gamma$  and various values of the particle-to-melt thermal conductivity ratio: (a)  $k_p/k_m = 0.1$ ; (b)  $k_p/k_m = 1.0$ ; (c)  $k_p/k_m = 10.0$ .

crystal–melt interface, by  $k_e$  that describes the contrast of the particle and melt thermal conductivities, and by  $N$  that characterizes the flow caused by the density change upon solidification.

Plots of the function  $u_p(\delta_0)$  for various values of  $\gamma$  and  $k_p/k_m$  are shown in figure 2 and figure 3 for the case when  $N = 0$ . One can see that the particle speed is small for both small and large  $\delta_0$  and reaches a maximum value at some intermediate value of  $\delta_0$ . Indeed, with the decrease of  $\delta_0$  the lubrication drag force increases faster than the van der Waals repulsion, thus slowing the particle. For large  $\delta_0$  the van der Waals repulsion decreases rapidly which also leads to the decrease of  $u_p$ . Recalling the definition of the velocity scale  $W$  in equation (3.4), we expect that the maximum particle speed is proportional to  $\lambda^{9/4} G^{1/4} R^{-1}$ . As described by Rempel & Worster (1999), larger particles placed in smaller temperature gradients are pushed away from the front more easily.

The effect of the crystal–melt surface energy on the particle velocity depends on the ratio of thermal conductivities. One can see from figure 2 that this effect is most pronounced when the two conductivities are equal. The effect of the surface energy is small for both  $k_p/k_m \ll 1$  and for  $k_p/k_m \gg 1$ . This is because in this case the shape of the interface is determined mainly by the distortion of the thermal field

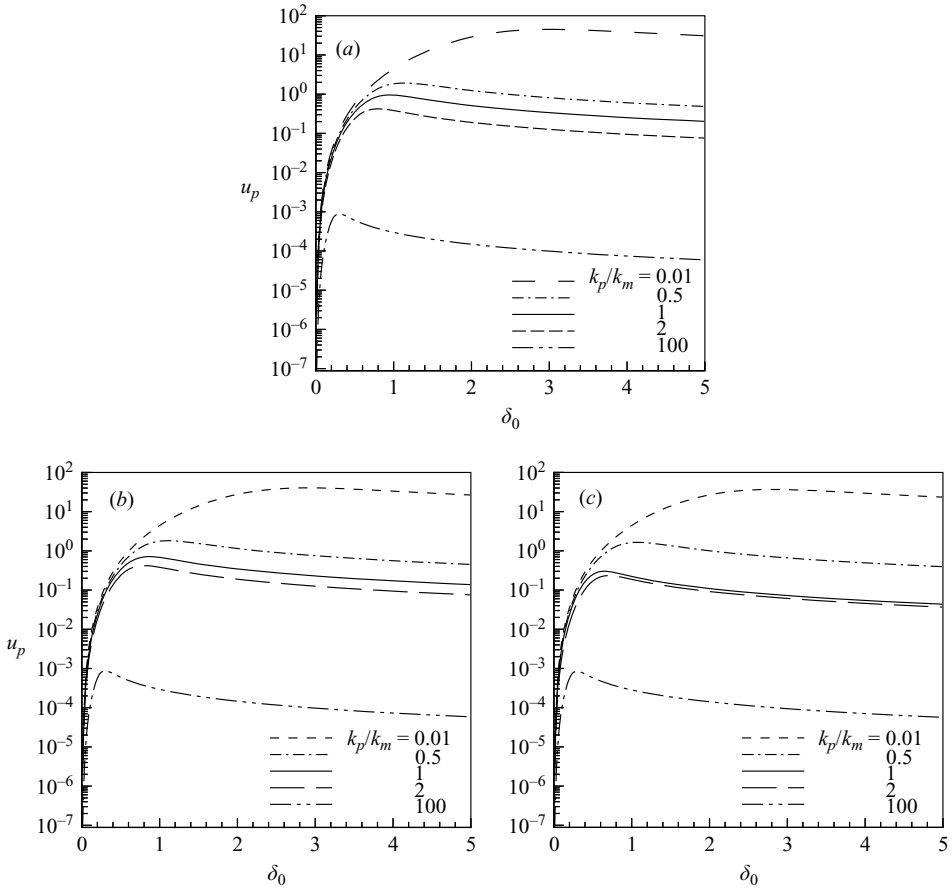


FIGURE 3. Dimensionless particle velocity  $u_p$  as a function of the dimensionless film thickness  $\delta_0$  for different values of the particle-to-melt heat conductivity ratio  $k_p/k_m$  and various values of the surface-energy parameter: (a)  $\gamma = 0$ ; (b)  $\gamma = 10.0$ ; (c)  $\gamma = 100.0$ .

around the particle near the solidification front (see below). One can see also that the increase of  $\gamma$  always leads to the decrease of the particle speed. The decrease of the maximal particle speed means that the particle will be engulfed by the front at lower solidification speeds. Therefore, one can conclude that the crystal–melt surface energy (Gibbs–Thomson effect) promotes particle engulfment.

From figure 3 one can see that the particle speed considerably decreases with the increase of  $k_p/k_m$ . This effect results from the distortion of the solidification front shape caused by the difference of the heat conductivities of the particle and the melt (see figure 4). For  $k_p/k_m < 1$ , the solidification front develops a bulge towards the particle so that the thickness of the liquid film between the particle and the front increases much more rapidly away from the particle base than in the case when the front is planar. This leads to the fast decay of the lubrication force that counteracts the particle repulsion by the van der Waals forces and to the larger speed of the particle away from the front. On the contrary, for  $k_p/k_m > 1$ , the temperature field leads to the distortion of the solidification front in such a way that a depression is formed near the particle (see figure 4). This is consistent with previous analyses by Chernov *et al.* (1977), Azouni & Casses (1998), and Garvin & Udaykumar (2003*a, b*,

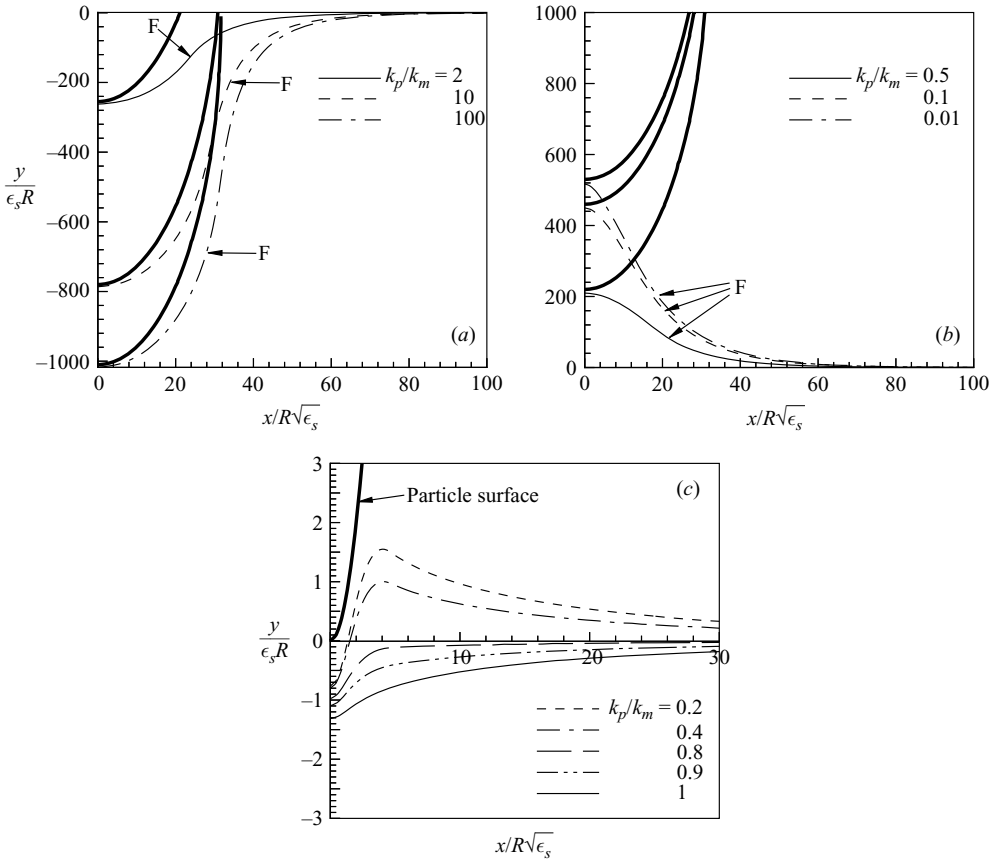


FIGURE 4. The shape of the solidification front near the base of the particle for several values  $k_p/k_m$  with (a)  $\gamma = 0.01$  and  $k_p/k_m > 1$ ; (b)  $\gamma = 0.01$  and  $k_p/k_m < 1$ ; (c)  $\gamma = 1.0$  and  $k_p/k_m \leq 1$ . The coordinates are the same as in figure 1. Thick lines in (a) and (b) show the particle surface, and F corresponds to the front. Panels (a) and (b) correspond to computations for  $\delta_0 = 1$  (fixed distance between the particle and the front), while (c) corresponds to  $b = 0$  (fixed position of the particle with respect to the undeformed front).

2004, 2005). In this case the thickness of the liquid film dividing the particle from the solid increases much more slowly away from the particle base than in the case of the planar front. This makes the lubrication forces decay much more slowly, and the total lubrication force that acts against the particle repulsion due to intermolecular forces increases considerably, thus yielding a smaller particle velocity away from the front. Therefore, one can conclude that for  $k_p > k_m$  particle engulfment is promoted (i.e. occurs at smaller speed of the solidification front). At the same time, we note that particle repulsion is still possible if the speed of the solidification front is small enough (less than the maximum particle speed), see below.

Figure 4 shows the shape of the solid-liquid interface near the base of the particle for two different values  $\gamma$  and several values of  $k_p/k_m$ . The horizontal coordinate is the distance from the base of the particle, scaled by  $\sqrt{\epsilon_s}R$ , while the vertical coordinate is the distance from the undeformed planar solidification front (far away from the base of the particle), scaled by  $\epsilon_s R$  (see also figure 1). The shape of the front does not depend on whether the particle is a solid sphere or a bubble since the front

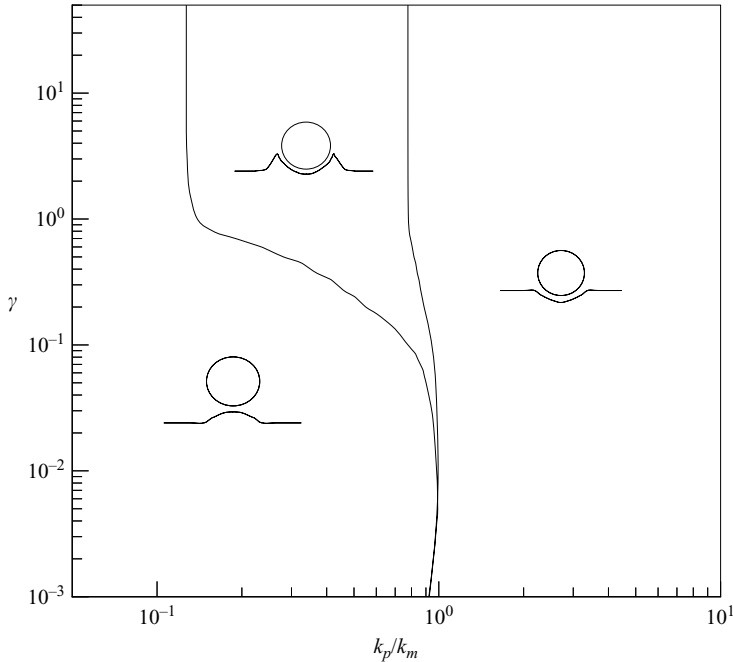


FIGURE 5. A diagram in the  $(k_p/k_m, \gamma)$ -plane showing the different types of solidification front shape with a particle near it.

deformation is determined by the effect of the disjoining pressure, surface energy, and conductivity difference described by (2.24) and (2.25). Figures 4(a) and 4(b) agree with the previous works by Shangguan *et al.* (1992) and Garvin & Udaykumar (2003a, b).

It is interesting to note the competing effects of large surface energy that tends to flatten the solid–liquid interface, and small particle-to-melt thermal conductivity ratio that tends to advance the interface towards the particle. This competition results in the interface shape shown in figure 4(c). The effect of  $\gamma$  is dominant near the base of the particle while the effect of  $k_p/k_m$  is dominant away from the particle for certain values of  $\gamma$  and  $k_p/k_m$ . We can hence distinguish three types of the interface shape: convex, concave, and concave–convex. Figure 5 shows the regions in the  $(\gamma$  vs.  $k_p/k_m)$  parameter plane in which three different types of interface shape are observed. When  $k_p/k_m > 1$  the shape of the interface is always concave, which promotes particle engulfment. For  $k_p/k_m < 1$  three regions exist, corresponding to a convex, concave–convex or concave interface. When  $\gamma$  is small, the domain corresponding to the concave–convex interface is confined to a narrow region close to  $k_p/k_m = 1$ , as was suggested by Sen *et al.* (1997). As  $\gamma$  increases this region becomes wider.

Finally, we note that crystallization-induced density change, described by the dimensionless parameter  $N$  in (3.6e), is simply reduced to the corresponding shift of the function  $u_p(\delta_0)$  up or down, depending on expansion ( $\rho_s < \rho_m$ ) or shrinkage ( $\rho_s > \rho_m$ ) of the solid phase with respect to the melt. For  $\rho_l > \rho_s$  ( $N > 0$ ) the density change produces flow away from the front that pushes the particle away so that its speed becomes larger than that without density change. Obviously, the speed is finite even for zero separation distance between the particle and the front. In the opposite case, when  $\rho_l < \rho_s$  ( $N < 0$ ), the flow produced by the density change is towards the front and pulls the particle in the same direction, thus decreasing its velocity away from the

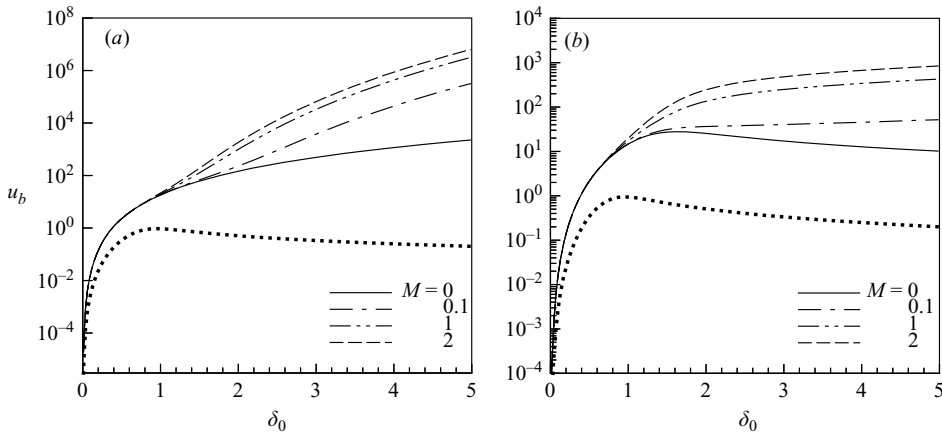


FIGURE 6. Dimensionless bubble velocity  $u_b$  as a function of the dimensionless film thickness  $\delta_0$  for various values of the Marangoni number  $M$  characterizing the thermocapillary effect, and for (a)  $k_p/k_m=0$ ; (b)  $k_p/k_m=0.1$ . The surface energy parameter  $\gamma=10$ . The dotted lines show the corresponding dependence for a particle with  $k_p/k_m=1.0$  and  $\gamma=0$  in the absence of the Marangoni effect.

front. For small separation distances  $\delta_0$ , this effect is dominant so that, if  $\rho_l < \rho_s$ , the particle velocity is always negative, i.e. the particle moves towards the front (in the lab frame).

The velocity of a bubble depends on the parameters  $\gamma$ ,  $k_e$ ,  $N$  as well as on the parameter  $M$  characterizing the thermocapillary effect. For  $N=M=0$  equation (3.5) gives  $u_b=4\epsilon u_1(\delta_0, \gamma, k_e)=4u_p$ . That is, in the absence of the thermocapillary effect and the bulk flow produced by density change upon solidification, the bubble speed is always four times larger than that of a solid particle for the same parameter values, due to the stress-free boundary condition at the bubble–liquid interface. All conclusions regarding the dependence of the particle velocity on the particle–front separation distance, surface energy parameter and conductivity ratio discussed above for the case of a solid particle remain the same for the case of a bubble, and the front deformation caused by a bubble is the same as that caused by a solid particle (of course, in the case of a bubble,  $k_p/k_m \ll 1$ ). Since the bubble-to-melt heat conductivity ratio is always small, the frontal deformation near the bubble will always lead to a bulge that will enhance the bubble repulsion due to decreased lubrication forces. Thus, for  $M=N=0$  the engulfment of a bubble will be suppressed in comparison with the engulfment of a solid particle.

In the presence of the thermocapillary effect ( $M > 0$ ) the bubble speed becomes even larger than  $4u_p$ . The imposed temperature gradient generates a gradient of surface tension at the bubble–liquid interface that leads to thermocapillary flow around the bubble and bubble migration in the direction of the temperature gradient. The bubble speed away from the front will therefore become larger than in the absence of the thermocapillary effect. Figure 6 shows the dimensionless bubble velocity  $u_b$  as a function of the dimensionless film thickness  $\delta_0$  for various values of  $M$  and two values of  $k_p/k_m$  (for comparison, the dotted lines show the speed of a solid particle with  $k_p/k_m=1$  and  $\gamma=0$ ). One can see that for  $M > 0$  the bubble speed is always larger than for  $M=0$ . For small  $\delta_0$  the speed change due to the thermocapillary effect is negligible since the lubrication and van der Waals forces dominate. However, for larger  $\delta_0$  the thermocapillary effect becomes more pronounced since the thermocapillary

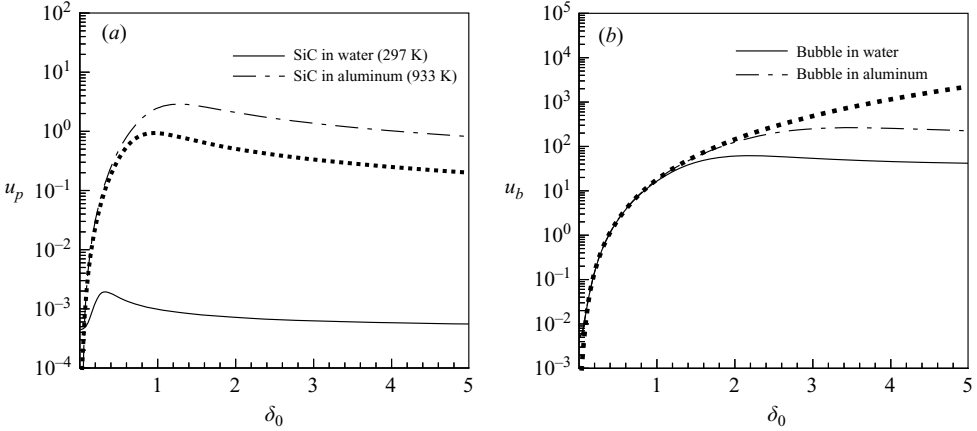


FIGURE 7. Dimensionless velocity  $u$  as a function of the dimensionless film thickness for some real systems for (a) a particle, (b) a bubble. The physical data are based on table 1. The dotted lines in (a) and (b) correspond to a solid particle with  $\gamma = 0$ ,  $k_p/k_m = 1$  and a bubble with  $\gamma = 0$ ,  $k_p/k_m = 0$ , respectively.

migration becomes the predominant mechanism of bubble motion. For small  $M$  the dependence  $u_b(\delta_0)$  is qualitatively the same as in the absence of the thermocapillary effect, and the bubble speed is maximal at some intermediate separation distance. With the increase of  $M$ ,  $u_b(\delta_0)$  becomes a monotonically increasing function: thermocapillary migration of the bubble becomes the predominant mechanism of bubble motion even at intermediate separation distances. One can conclude therefore that the thermocapillary effect suppresses bubble engulfment by an advancing solidification front. Note that when the separation distance between the bubble and the solid-liquid interface becomes large enough the lubrication approximation fails; far from the solidification front the bubble speed tends to a constant value corresponding to thermocapillary migration (Young *et al.* 1959). Also note that in the presence of Marangoni effect, the bubble speed at separation distances  $\delta_0 > 1$  is quite sensitive to the ratio  $k_p/k_m$ .

Figure 7 shows examples of  $u_p(\delta_0)$  for a solid particle (figure 7a) and  $u_b(\delta_0)$  for a gas bubble (figure 7b) for sets of physical parameters corresponding to some real physical systems. The system parameters are summarized in table 1. For comparison, the dotted line in figure 7(a) corresponds to  $u_p(\delta_0)$  computed by Rempel & Worster (1999) that takes into account the effect of van der Waals repulsion balanced by the lubrication force while other effects, such as the surface energy, the bulk flow produced by the density change, and the heat conductivity difference, are neglected. One can see that such an approximation can lead to orders of magnitude difference in particle speed. Similarly, in figure 7(b), the dotted line shows  $u_b(\delta_0)$  for a bubble with  $\gamma = 0$  and  $k_p/k_m = 0$ . One can see that while for small separation distances such an approximation would work fairly well, for larger separation distances it gives an orders of magnitude over-estimation of the bubble speed.

## 6. Conclusions

We have analytically investigated the behaviour of a solid particle and a gas bubble near an advancing solidification front by means of asymptotic analysis using the lubrication approximation. We have considered a general formulation of the problem in which the most important physical effects that influence the particle speed near the



solidification front are present together: van der Waals repulsion forces, lubrication forces, crystal–melt surface energy, heat conductivity difference, density change upon phase transition, as well as the thermocapillary effect in the case of a bubble. We have computed the dimensionless particle speed as a function of the dimensionless gap between the particle and the front, as well as of several dimensionless parameters that characterize the described effects. In most cases the particle speed has a maximum at a certain separation distance and tends to zero at both zero and infinite separation distances. However, in the case of a bubble with the thermocapillary effect, the maximum can disappear and the dependence can become monotonically increasing, although tending to an asymptotic value corresponding to stationary thermocapillary migration of the bubble. Also, the speed of the particle (in the lab frame) can be non-zero at zero separation distance if the flow caused by the density change upon solidification is present.

These results allow one to predict the conditions for particle engulfment by the front which are schematically shown in figure 8. Here, the horizontal line corresponds to the speed of the solidification front,  $V$ . For a typical dependence with a maximum, if  $V < u_{max}$ , there are two steady-state positions of a particle near the front: stable,  $\delta_s$ , and unstable,  $\delta_u$  (see figure 8a). If the initial position  $\delta_u < \delta_0 < \delta_s$ , then  $u > V$  and the particle will move away from the front, approaching the steady-state separation distance,  $\delta_s$ . With this distance unchanged, it will be further pushed in the melt in front of the advancing solid–liquid interface. If  $\delta_0 > \delta_s$ , the front, moving faster than the particle, will catch up with it, with the separation distance between them approaching  $\delta_s$ ; at this stage the front will continue to push the particle in front of it. If  $\delta_0 < \delta_u$ , then  $u < V$  and the front will reach the particle in a finite time and engulf it. If the front is moving so fast that  $V > u_{max}$ , no steady-state separation distance exists and, regardless of the initial separation distance, the particle will be engulfed by the front. Regions in the  $(u, \delta_0)$ -plane corresponding to particle repulsion and engulfment are shown in the figure.

If the bulk flow away from the front, produced by the density decrease upon solidification, is present, the typical engulfment diagram is as shown in figure 8(b). It is similar to the one shown in figure 8(a), except that in this case a particle can be captured by the solidification front only if the solidification speed is larger than the minimal one corresponding to the lower horizontal line in figure 8(b).

In the case of a bubble with the thermocapillary effect, the dependence  $u_{max}(\delta_0)$  qualitatively changes with the increase of the Marangoni number and can have the forms shown in figures 8(c, d). The dashed line qualitatively shows the limit when the lubrication approximation fails and the bubble speed tends to the thermocapillary migration speed,  $U_{TM}$ , computed by Young *et al.* (1959). If the dependence  $u_{max}(\delta_0)$  is as shown in figure 8(c), then, in a certain interval of the solidification front speed,  $u_{max} < V < u_{min}$ , there can be three steady states (one stable and two unstable). Outside this interval there is only one, unstable steady state for  $V < u_{min}$  and  $u_{max} < V < U_{TM}$ , and no steady states for  $V > U_{TM}$ . Thus, for example, if the front speed is in the interval with three steady states (see figure 8b) and the initial separation distance between the bubble and the front  $\delta_0 < \delta_{u1}$  the front will catch up with the bubble and engulf it in a finite time. If  $\delta_{u1} < \delta_0 < \delta_{u2}$  then, depending on the initial position, the bubble will approach the steady-state separation distance  $\delta_s$  by either moving away from the front (for  $\delta_{u1} < \delta_0 < \delta_s$ ) or towards the front (for  $\delta_s < \delta_0 < \delta_{u2}$ ) and will be further pushed by the moving front at this distance. If  $\delta_0 > \delta_{u2}$  the bubble will always move away from the front since the thermocapillary migration speed will be larger than the speed of the solid–liquid interface. If the frontal speed  $V < u_{min}$  or  $u_{max} < V < U_{TM}$  there is only one, unstable steady state,  $\delta_u$ , such that if  $\delta_0 < \delta_u$  the

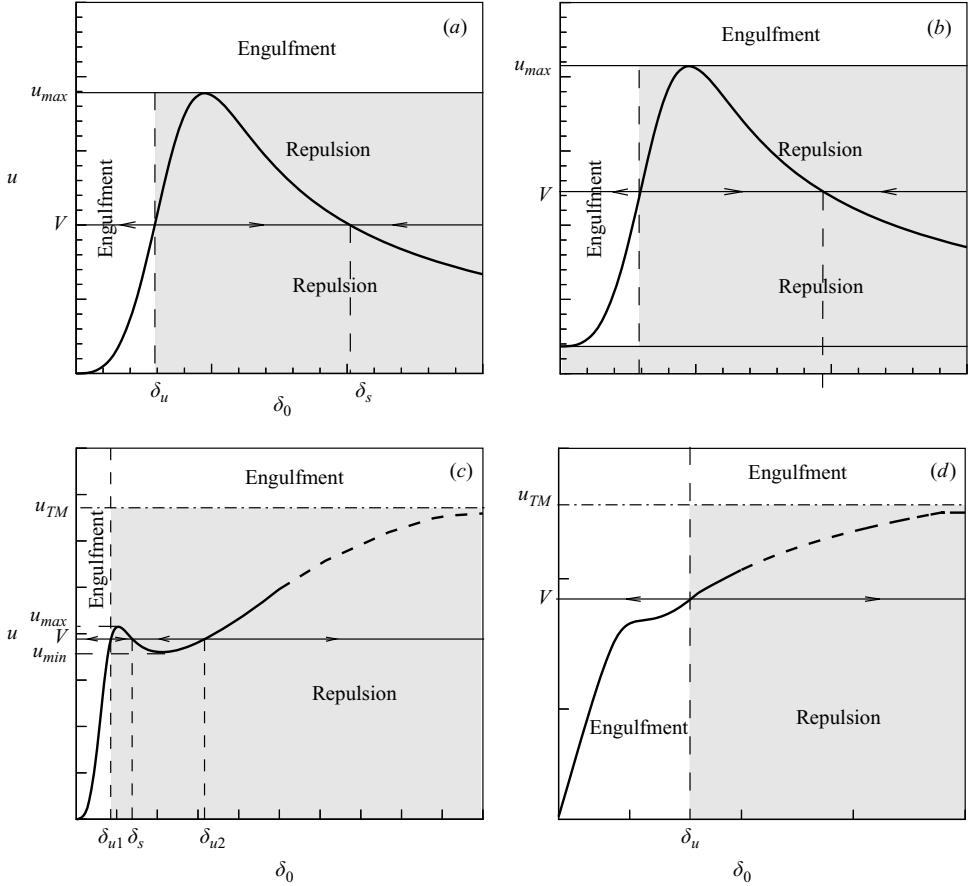


FIGURE 8. Schematic representation of engulfment conditions based on the dependence of a particle or bubble dimensionless speed on the dimensionless separation distance from the front,  $u(\delta_0)$ : (a) typical dependence with one maximum ( $\delta_u$  – unstable steady state,  $\delta_s$  – stable steady state); (b) for a solid particle in the presence of the bulk flow caused by the density change upon solidification; (c) for a bubble with thermocapillary effect with two extrema (dashed line corresponds to an asymptotic value of thermocapillary migration speed which is beyond the validity of the lubrication approximation); (d) monotonic dependence for a bubble with thermocapillary effect for large Marangoni numbers.

bubble will be engulfed by the front, and if  $\delta_0 > \delta_u$  the bubble will escape from the front, always moving away from it. If  $V > U_{TM}$ , no steady state exists and, regardless of the initial separation distance, the bubble will be engulfed by the solidification front that is moving faster than the maximum possible bubble speed,  $U_{TM}$ . With further increase of the Marangoni number the dependence of the bubble speed on the separation distance becomes monotonically increasing, as shown in figure 8(d). In this case, for  $V < U_{TM}$  there is only one, unstable steady state,  $\delta_u$ , such that if  $\delta_0 < \delta_u$ , the front catches up with the bubble in a finite time and engulfs it, and if  $\delta_0 > \delta_u$ , the bubble, driven by the thermocapillary effect, moves along the temperature gradient away from the front and can never be captured by the solid phase. However, for  $V > U_{TM}$  there is no steady state since the frontal speed is larger than the maximum possible speed of the bubble so that the bubble will be engulfed by the solid phase regardless of its initial position.

We have examined the relative role of various effects in the interaction between a particle and an advancing solidification front. We have shown that the surface energy of the solid–liquid interface promotes particle engulfment in that the critical solidification speed at which the front captures the particle decreases with the increase of the surface energy. The flow produced by the density change upon solidification can affect the interaction in both ways: it promotes engulfment when the solid is more dense than the melt, and it facilitates capture when the solid is less dense. However, the strongest effect is made by the difference of heat conductivities between the particle and the melt. In the case of a small particle-to-melt conductivity ratio the particle is more easily repulsed by the front. If the ratio is large, the particle is easily engulfed by the front.

We have estimated the speed of a particle near a solidification front for some real liquid–solid–gas systems. We have found that incorporation of all the described effects can change the particle speed by almost one order of magnitude in comparison with that computed by Rampel & Worster (1999, 2001) who took into account only the effects of the surface energy, van der Waals interactions and lubrication pressure.

We have also computed the shape of the solidification front. We have shown that the two most important parameters affecting its shape are the solid–liquid surface energy and the particle-to-melt heat conductivity ratio. We have found regions in the surface energy–conductivity ratio parameter plane that correspond to qualitatively different shapes of the solidification front near the particle: concave, convex, and concave–convex (see figure 5).

The obtained dependences of the particle speed on the separation distance from the solidification front and various physical parameters allow us to find regions in the parameter space where a particle will be engulfed by an advancing solidification front regardless of its initial position. As described above, for this to happen the solidification front speed must be larger than the maximum possible speed of the particle corresponding to  $u_{max}$ , or  $U_{TM}$  in the case of a bubble in the presence of the thermocapillary effect for some parameter values. Examples of such regions in different parameter planes are shown in figure 9. The solid line in figure 9(a) corresponds to the level set of the function  $u_{max}(\gamma, k_p/k_m) = u_{max}(0, 1) = \text{const}$  (for  $N = 0$ ), where  $u_{max}(\gamma, k_p/k_m)$  is the maximum of the function  $u_p(\delta_0, \gamma, k_p/k_m)$  defined by (4.2) (see also figures 2 and 3). One can see from figure 9(a) that if the *dimensionless* speed of the solidification front equals to some constant value ( $u_{max}(0, 1)$  in the case shown in figure 9a) then, depending on the dimensionless surface energy  $\gamma$  or the conductivity ratio  $k_p/k_m$ , a particle will be either always engulfed by the front or repelled by it if the initial separation distance is larger than the threshold value (see figure 8). Obviously, the solid line in figure 9(a) passes through the point  $\gamma = 0$ ,  $k_p/k_m = 1$  corresponding to the reference values of  $u_{max}$  chosen for this figure.

The critical engulfment condition  $V = u_{max}(\gamma, k_p/k_m)$  is equivalent to the following relation for the dimensional parameters:

$$V^* = \frac{1}{6\mu R} \left[ \frac{L_v A^3 G}{(6\pi)^3 T_m} \right]^{1/4} u_{max}(\gamma, k_p/k_m), \quad (6.1)$$

where  $V^*$  is the dimensional speed of the solidification front, and

$$\gamma = \frac{T_m \sigma}{L_v G R^2}. \quad (6.2)$$

Relations (6.1)–(6.2) allow one to determine regions in the planes of physical parameters in which a particle or a bubble will always be engulfed by an advancing solidification front. Examples of such regions for an SiC particle in water are shown

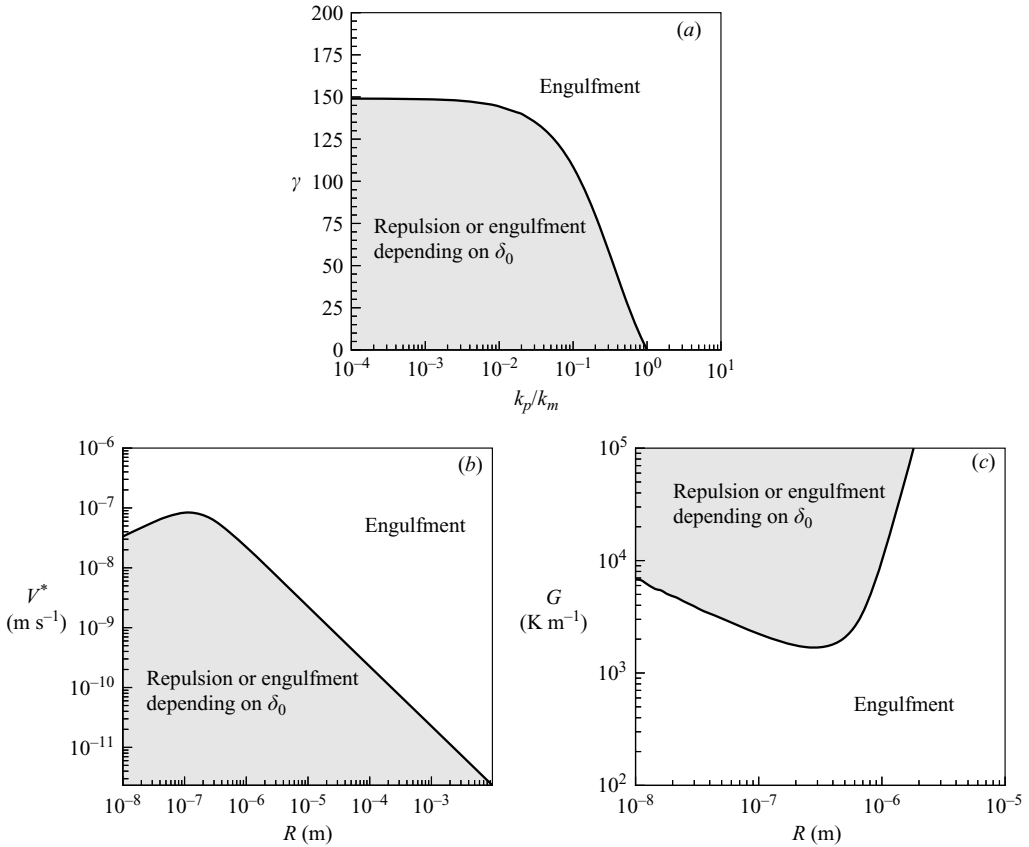


FIGURE 9. Regions in parameter planes corresponding to engulfment or repulsion of a solid particle by a moving solidification front. (a) Regions in the  $(\gamma, k_p/k_m)$ -parameter plane corresponding to engulfment of a solid particle (white) and its repulsion or engulfment, depending on the initial position (shaded); repulsion occurs for sufficiently large separation distance  $\delta_0$ . (b) Conditions for engulfment of an SiC solid particle with radius  $R$  in water by a freezing front moving with speed  $V^*$ ; other physical parameters are given in table 1. (c) Conditions for engulfment of a solid SiC particle with radius  $R$  in water by a freezing front moving with a constant speed shown in table 1 and thermal gradient  $G$ ; other physical parameters are given in table 1.

in figure 9(b, c). Figure 9(b) shows conditions for engulfment of a particle with radius  $R$  by a front moving with speed  $V$ ; the thermal gradient as well as other physical parameters are given in table 1. The white region corresponds to particle engulfment regardless of its initial position. The shaded region corresponds to particle repulsion or engulfment, depending on the initial separation distance between the particle and the front (see above). For a particle with radius  $R$  there is a critical solidification front speed above which this particle will always be captured by the moving front. One can see that in the particular case shown in figure 9(b) the critical solidification speed reaches a maximum value of about  $0.01 \mu\text{m s}^{-1}$  for a particle with the radius of about  $1 \mu\text{m}$ , so that if the speed of the solidification front is larger than this critical value, a particle of any size will be captured by it. Such a small value of the critical engulfment solidification speed is due to a very large particle-to-melt heat conductivity ratio in the SiC–water system. Figure 9(c) shows critical values of the applied thermal gradient below which a particle with the radius  $R$  will be engulfed regardless of its

initial position with respect to the front. The figure corresponds to an SiC particle in water when the freezing front is moving with the speed  $V^* = 1.25 \times 10^{-8} \text{ m s}^{-1}$ . One can see that in this case the critical thermal gradient has a minimum value about  $100 \text{ K cm}^{-1}$  when the particle radius is about  $1 \mu\text{m}$ . If the applied thermal gradient is below the minimal then a particle will always be captured by the solid phase. If the thermal gradient is above the minimal value then a particle whose radius is in a certain interval will be repelled by the front (provided it is initially far enough from it) but both smaller and larger particles will be engulfed by the front.

Finally we note that in the diagrams shown in figure 9 the bulk flow produced by the density change upon solidification is not taken into account. It can be shown, however, that in the particular systems presented in figure 9 this effect changes the critical parameter values by no more than a few percent. Also, for water and aluminium, thermal conductivities of the liquid and crystalline phases differ by at least a factor of two. Although the theory presented in this paper is valid for the case when the thermal conductivities of the crystal and melt are equal, their difference should not qualitatively change the main conclusions of our analysis.

We are grateful to Dr Brian Tsai for his early work on this problem. We are also very grateful to anonymous referees of our paper for numerous very helpful suggestions that led to significant improvement of this paper.

## Appendix

For the case when  $\gamma = 0$  the integrals (3.6a)–(3.6d) can be evaluated analytically by introducing a new variable,  $\delta(\theta)$ , instead of  $\theta$ , and computing  $d\delta/d\theta$  by using implicit differentiation of (3.3). As a result one obtains the following analytical expressions for the functions  $u_1(\delta_0, 0, k_e)$  and  $u_2(\delta_0, 0, k_e)$ :

$$u_1(\delta_0, 0, k_e) = \left( \frac{A_1}{2\delta_0^2} + \frac{A_2}{2\delta_0^6} \right) \left( \frac{B_1}{2\delta_0} + \frac{2B_2}{5\delta_0^5} + \frac{B_3}{6\delta_0^9} \right)^{-1},$$

$$u_2(\delta_0, 0, k_e) = A_3 \left( \frac{B_1}{2\delta_0} + \frac{2B_2}{5\delta_0^5} + \frac{B_3}{6\delta_0^9} \right)^{-1},$$

where

$$A_1 = \frac{1 - 2k_e}{(k_e + 1)^3}, \quad A_2 = \frac{1}{(k_e + 1)^2}, \quad A_3 = \frac{4k_e^3 + 26k_e^2 + 4k_e + 15}{36(k_e + 1)^4},$$

$$B_1 = \frac{(2k_e - 1)^2}{(k_e + 1)^5}, \quad B_2 = \frac{1 - 2k_e}{(k_e + 1)^4}, \quad B_3 = \frac{1}{(k_e + 1)^3}.$$

## REFERENCES

- AZOUNI, M. A. & CASSES, P. 1998 Thermophysical properties effects on segregation during solidification. *Adv. Colloid Interface Sci.* **75**, 38–106.
- BAGDASAROV, K. S., OKINSHEVICH, V. V. & KHOLOV, A. 1980 On the theory of capture of gas bubbles by a crystal growing from the melt. *Phys. Stat. Sol.* **58**, 317–322.
- BRONSTEIN, V. L., ITKIN, Y. A. & ISHKOV, G. S. 1981 Rejection and capture of cells by ice crystals on freezing aqueous solutions. *J. Cryst. Growth* **52**, 345–349.
- CATALINA, A. V., MUKHERJEE, S. & STEFANESCU, D. M. 2000 A dynamic model for the interaction between a solid particle and an advancing solid/liquid interface. *Metall. Trans. A* **31**, 2559–2568.
- CHERNOV, A. A., TEMKIN, D. E. & MEL'NIKOVA, A. M. 1976 Theory of the capture of solid inclusions during the growth of crystals from the melt. *Sov. Phys. Crystallogr.* **21**, 369–373.

- CHEKHOV, A. A., TEMKIN, D. E. & MEL'NIKOVA, A. M. 1977 The influence of the thermal conductivity of a microparticle on its capture by a crystal growing from a melt. *Sov. Phys. Crystallogr.* **22**, 656–658.
- CISSE, J. & BOLLING G. F. 1971 A study of the trapping and rejection of insoluble particles during the freezing of water. *J. Cryst. Growth* **10**, 67–76.
- CORTE, A. E. 1962 Vertical migration of particles in front of a moving freezing plane. *J. Geophys. Res.* **67**, 1085–1090.
- DZYUBA A. S. & ZU Y. Y. 1986 Interaction of gas bubble with melt crystallization front. *Sov. Phys. Crystallogr.* **30**, 684–686.
- GARVIN, J. W. & UDAYKUMAR, H. S. 2003a Particle-solidification front dynamics using a fully coupled approach, part I: methodology. *J. Cryst. Growth* **252**, 451–466.
- GARVIN, J. W. & UDAYKUMAR, H. S. 2003b Particle-solidification front dynamics using a fully coupled approach, part II: comparison of drag expressions. *J. Cryst. Growth* **252**, 467–479.
- GARVIN, J. W. & UDAYKUMAR, H. S. 2004 Drag on a particle being pushed by a solidification front and its dependence on thermal conductivities. *J. Cryst. Growth* **267**, 724–737.
- GARVIN, J. W. & UDAYKUMAR, H. S. 2005 Drag on a ceramic particle being pushed by a metallic solidification front. *J. Cryst. Growth* **276**, 275–280.
- GEUZIN YA. E. & DZYUBA A. S. 1981 Crystallization of a gas-saturated melt. *J. Cryst. Growth* **52**, 337–344.
- GILPIN, R. R. 1980 Theoretical studies of particle engulfment. *J. Colloid Interface Sci.* **74**, 44–63.
- HADJI, L. 1999 Asymptotic analysis of particle engulfment. *Phys. Rev. E* **60**, 6180–6183.
- HADJI, L. 2002 Axisymmetric shapes and force resulting from the interface of a particle with a solidifying interface. *Phys. Rev. E* **66**, 041404.
- ISRAELACHVILI, J. 1992 *Intermolecular and Surface Forces*. Academic.
- JOHANSEN, S. T. & TANIGUCHI, S. 1998 Prediction of agglomeration and break-up of inclusions during metal refining. *The minerals, Metall. Mat. Soc.* 855–861.
- KÖRBER, C. 1988 Phenomena at the advancing ice-liquid interface: solutes, particles and biological cells. *Q. Rev. Biophys.* 229–298.
- ONODA, G. Y. 1985 Direct Observation of two-dimensional, dynamical clustering and ordering with colloids. *Phys. Rev. Lett.* **55**, 226–229.
- REMPEL, A. W. & WORSTER M. G. 1999 The interaction between a particle and an advancing solidification front. *J. Cryst. Growth* **205**, 427–440.
- REMPEL, A. W. & WORSTER M. G. 2001 Particle Trapping at an advancing solidification front with interfacial-curvature effects. *J. Cryst. Growth* **223**, 420–432.
- SEN, S., KAUKLER, W. F., CURRERI, P. & STEFANESCU D. M. 1997 Dynamics of Solid/Liquid Interface Shape Evolution near an Insoluble Particle – An X-ray Transmission Microscopy Investigation. *Metall. Trans. A* **28**, 2129–2135.
- SHACKELFORD, J. F. & ALEXANDER, W. (Eds.) 2000 *CRC Materials Science and Engineering Handbook*, 3rd Edn. CRC Press.
- SHANGGUAN, D., AHUJE, S. & STEFANESCU, D. M. 1992 An analytical model for the interaction between an insoluble particle and an advancing solid/liquid interface. *Metall. Trans. A* **29**, 1697–1706.
- STEFANESCU D. M., JURETZKO F. R., DHINDAW, B. K., CATALINA, A., SEN, S. & CURRERI P. A. 1998 Particle Engulfment and pushing by solidifying interfaces: Part II. microgravity experiments and theoretical analysis. *Metall. Trans. A* **29**, 1697–1706.
- UHLMANN, D. R., CHALMERS, B. & JACKSON, K. A. 1964 Interaction between particles and a solid–liquid interface. *J. Appl. Phys.* **35**, 2986–2993.
- WANG Z., MUKAI, K. & LEE, I. J. 1999 Behavior of fine bubbles in front of the solidifying interface. *ISIJ Intl* **39**, 553–562.
- WETTLAUFER, J. S., WORSTER, M. G., WILEN, L. A. & DASH, J. G. 1996 A theory of pre-melting dynamics for all power law forces. *Phys. Rev. Lett.* **76**, 3602–3605.
- WILEN, L. A., WETTLAUFER, J. S., ELBAUM, M. & SCHICK, M. 1995 Dispersion-force effects in interfacial melting of ice. *Phys. Rev. B* **52**, 12426–12433.
- YOUNG, N. O., GOLDSTEIN, J. S. & BLOCK, M. J. 1959 The motion of bubbles in a vertical temperature gradient. *J. Fluid Mech.* **6**, 350–356.
- ZUBKO, A. M., LOBANOV, V. G. & NIKONOVA, V. V. 1973 Reaction of foreign particles with a crystallization front. *Sov. Phys. Crystallogr.* **18**, 239–241.